Experimental and numerical study of waves breaking over a submerged three-dimensional bar

Arun Kamath*[1], Travis Roy[2], Betsy Seiffert[1], and Hans Bihs[1]

[1]Department of Civil and Environmental Engineering, Norwegian University of Science and Technology (NTNU), 7491 Trondheim, Norway
[2]Department of Ocean & Mechanical Engineering, Florida Atlantic University, Boca Raton, FL, USA

Journal of Waterway, Port, Coastal and Ocean Engineering, 2021, , pp. .
DOI: http://dx.doi.org/10.1061/(ASCE)WW.1943-5460.0000697

Abstract

Depth-induced breaking is the major wave transformation process in the coastal waters that significantly influences the wave energy that eventually reaches the coastline. Most of the studies on depth-induced wave breaking focus on evaluating the wave breaking characteristics on a slope or a reef in two-dimensions, accounting for the reduction of water depth in the direction of wave propagation. The current study investigates wave breaking on a three-dimensional submerged bar through experiments and numerical simulations. Propagation of non-breaking and breaking waves in different water depths is studied and the energy transferred across the wavefront due to the presence of a side slope and the non-simultaneous breaking over wavefront is analysed. The results indicate that classification criteria that account for the local water depth can reasonably predict the type of breaking. The long period waves in the study that did not break over the structure are most effected by refraction. It is also found that the extent of the domain where a steep wave crest is seen increases from non-breaking to spilling to plunging breaking waves. In the case of the non-breaking waves, this steep crest propagates along the domain without breaking.

Keywords: breaking waves; three-dimensional; 3D; CFD; computational fluid dynamics; submerged bar; REEF3D

*Corresponding author, arun.kamath@ntnu.no

Postprint, published in Journal of Waterway, Port, Coastal and Ocean Engineering, doi: http://dx.doi.org/10.1061/(ASCE)WW.1943-5460.0000697

1 Introduction

Depth-induced wave breaking is one of the most important wave transformation processes in the coastal waters that significantly influences other coastal processes such as near-shore currents, wave run up, sediment transport and beach morphodynamics. In order to quantify the process of wave breaking, several parameters such as the Irribarren number, breaker type, breaker depth and height indices are used. Current literature consists of several studies where depth-induced wave breaking and its effects are studied in detail. Wave breaking over plane slopes, submerged bars and reefs have been widely studied though experiments (Battjes, 1974; Kjeldsen and Myrhaug, 1978; Smith and Kraus, 1990; Beji and Battjes, 1993; Ting and Kirby, 1996; Johnson, 2006; Blenkinsopp and Chaplin, 2008) and different parameters to quantify the type of breaking, establish a relationship between the incident wave and the breaking wave properties have been proposed. Large scale experiments have studied wave breaking and sediment transport due to breaking waves. Further knowledge regarding wave breaking and linked coastal processes is obtained through large scale field measurements to quantify the turbulent kinetic energy energy under breaking waves (Sutherland and Melville, 2015) and LiDAR measurements to measure energy dissipation in the swash zone (Martins et al., 2018).

Numerical investigations of breaking waves have been carried out using models of varying degrees of fidelity focusing on different processes in the swash zone. Models based on shallow water equations and Boussinesq equations provide a good approximation of the wave transformation process (Grilli et al., 2001; Stelling and Zijlema, 2003). With advances in computational methods and computational power, advanced modelling techniques employing the Reynolds-averaged Navier-Stokes equations are used to represent the overturning wave crest and quantify the breaking wave characteristics accurately (Alagan Chella et al., 2019; Aggarwal et al., 2019*a*; Liu et al., 2020; Larsen et al., 2020). While these studies have added a large amount of new knowledge to literature, they consider a two-dimensional obstacle with the process of shoaling occurring along the seaward slope, resulting in wave breaking either on the slope, the crest of the slope or the flat bed that follows after.

An interesting and highly relevant aspect that remains largely unexplored is the interaction of waves with a three-dimensional obstacle and the wave breaking due to such an interaction. Such a scenario is closer to a realistic field scenario with complex bathymetry. A regular side slope provides more insight into the wave breaking process with influence from all three spatial dimensions, albeit, under controlled conditions compared to field measurements. The asymmetry in the bottom topography resulting in asymmetrical energy transfer and wave breaking can provide more insight into the three-dimensional wave breaking process.

The current study investigates the wave breaking process on a more complex bottom topography than that used in two-dimensional experimental and numerical investigations by including a slope in the direction normal to the principal direction of wave propagation. The experimental setup is designed through a preliminary numerical investigation using the open-source CFD model REEF3D (Bihs et al., 2016) and experimental investigations are carried out at the Florida Atlantic University (FAU) – SeaTech wave flume (Roy, 2018). The measurements are then used to validate the numerical model and further studies are carried out. The investigation encompasses three different water depths with six different incident waves each. The paper is organised as follows. The wave breaking characteristics are studied from the measurements and compared to analytical predictions. A grid convergence and validation

study is presented. Fifteen numerical simulations are carried out with a wider domain for different types of wave breaking. This is followed by an investigation into wave decomposition and wave energy distribution in the domain using spectral analysis. Furthermore, the visualisation from the simulations are used to study the combined refraction and breaking phenomenon. The rotation of the wavefront and the width of the overturning crest are investigated. The analysis is organised in groups of three waves of different water depths based on the wave breaking observed in the experiments. Five such groups are formed in this manner- one group of non-breaking waves, two groups of spilling breaking waves and two groups of plunging breaking waves.

2 Experimental investigation

The flume used in the experiments is 18.30 m long, 1.237 m wide, and 1.20 m tall. The tank side walls are made of plexiglass allowing for visual observations. Wave generation in the flume for the experiments are carried out using a flap type wavemaker placed approximately 1.22 m from the starting wall, the mechanical system for the wavemaker moves by use of a rigid rotating disk and arm combination connected to the paddle component. A submerged bar is installed in the flume after considering previous studies conducted in the same flume (Kouvaras and Dhanak, 2018) and pre-trial simulations using a CFD-based numerical model (Aggarwal et al., 2019*b*). The dimensions of the three-dimensional submerged bar are shown in Fig. (1). The submerged bar has a seaward slope and leeward slope of 1:6.933. The plateau region in between is 2.439 m long. In order to induce three-dimensional wave breaking, a sloping side is built on one side of the flume with a slope of 1:0.963. The submerged bar is constructed with a combination of U-bar and L-Bar 6061 aluminium framing connected together with aluminium nut and bolt connections. The free surface elevation data is collected using a configuration of four wave gauges. The array of gauges was mounted to a wood span with C-clamps and positioned laterally across the top of the wave flume. The lateral array positioning is used to study the variation of the waveforms in the lateral (y-axis) direction due to the three-dimensional submerged bar geometry. The locations of the wave gauges are carefully measured in reference to the submerged bar. The positions of wave gauge arrays are shown in Fig.(2). The locations of arrays #1, #2, #4, and #5 are held constant for all cases, whereas array #3 is moved such that is it located just before the waves become unstable before wave breaking. It is not possible to standardise the location of array #3 for all runs since the waves have varying breaking positions which could be identified only during post-processing. An overview of the input conditions in the experiments is presented in Table (1).

Table 1: Input parameters for experiments

Case	Water depth, d (m)	Period, T_0 (s)	Wave height H_0 (m)
A (1-6)	0.52	1.36- 3.93	0.019- 0.078
B (1-6)	0.55	1.28- 3.20	0.024- 0.094
C (1-6)	0.58	1.21- 2.87	0.031- 0.10

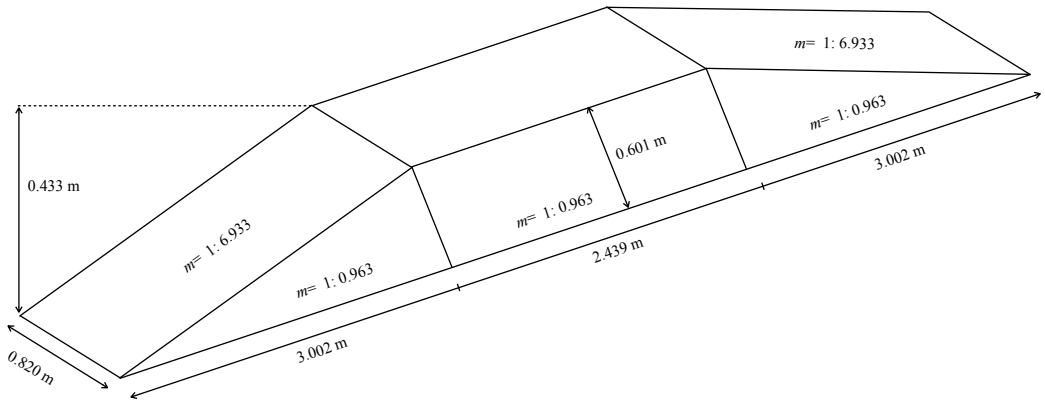

Figure 1: Dimensions of the three-dimensional submerged bar used in the study

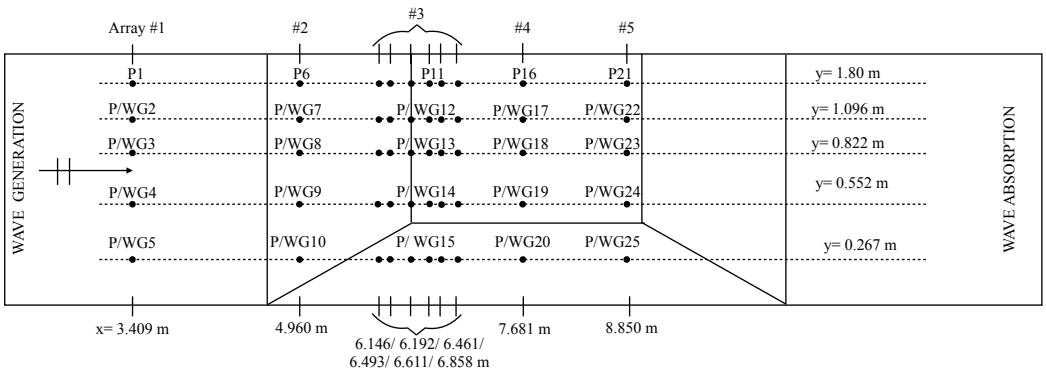

Figure 2: Locations of the wave gauges in the wave tank

3 Numerical Modelling

The numerical modelling of the three-dimensional wave breaking process is carried out using the open-source CFD model REEF3D. The model solves the two-phase fluid flow problem using the Reynolds-averaged Navier-Stokes (RANS) equations in a finite difference framework. The level set method is used to obtain the interface between air and water. The turbulence in the flow is modelled using the two equation k-ω model with eddy viscosity limiters (Menter, 1992). In addition to avoid overproduction of turbulence around the free surface, a boundary condition is used for the specific turbulence dissipation (Naot and Rodi, 1982) as demonstrated for the current model in Alagan Chella et al. (2016) for spilling and plunging breaking waves and for other complex free surface deformations by Kamath et al. (2019).

The numerical wave tank (NWT) is 18.0 m long, 1.237 m wide and 1.0 m high to emulate the wave flume used in the experiments. The relaxation method (Engsig-Karup et al., 2008) for wave generation is used, with a 3 m long relaxation zone. The waves are absorbed at the end of the tank using an active absorption method. Such a combination is optimal for the wave tank with accurate wave generation and low reflection from the beach, along with computational efficiency (Miquel et al., 2018). A submerged bar is placed in the numerical wave tank matching the dimensions of the structure in the experiments with the seaward toe 3.459 m from the wave generation zone. A length of 6.098 m is available from the leeward toe of the submerged bar to the end of the domain where active absorption is enabled. Free surface elevations are calculated at the same locations in the NWT (P) as in the experiments (WG). A non-uniform grid is used in the study. A grid stretching method is used to obtain finer grids in the region of wave breaking region and in the vicinity of the free surface. A grid convergence study is performed, the model is validated and additional simulations are then carried out. The input parameters for wave generation are the same as those in the experiments. To avoid the influence of the wall effects due to the relatively narrow physical flume used in the study, simulations for the analysis are carried out using a wider domain with $y_{max} = 2.0$ m. The simulations for the validation of the numerical model use the narrower flume following the experimental setup.

4 Results and discussion

4.1 Wave breaker classification from experiments

Based on the offshore values of the wave heights and wave periods of the wave generated in the experiments, three different classification criteria proposed by Galvin (1969), Smith and Kraus (1990) and Yao et al. (2013) for wave breaking over two-dimensional bars and reefs are used and compared to the observations from the current experiments with a three-dimensional structure. Non-breaking waves can be predicted only using the criteria proposed by Yao et al. (2013) which is based on the deep water wave height (H_0) and the still water depth on the reef (h_r). This predicts plunging breaking for $h_r/H_0 < 1.8$, spilling breaking for $1.8 \geq h_r/H_0 \leq 2.8$ and no breaking for $h_r/H_0 > 2.8$. The wave characteristics and the breaking wave classification for cases with $d = 0.52$ m, $d = 0.55$ m and $d = 0.58$ m are presented in Tables 2, 3 and 4 respectively. It is seen that the prediction using the criteria proposed by Galvin (1969) predicts plunging wave breaking for all the cases. The criteria proposed by Smith and Kraus (1990) predict the plunging correctly whereas the

observed spilling breakers are classified as surging breakers. The predictions using the criteria proposed by Yao et al. (2013) agree with most of the observations in the current study except for C3-C6. In C4, with $d = 0.58$ m, $T_0 = 1.817$ s and $H_0 = 0.052$ m, non-breaking waves are predicted. In this case, the breaking waves are observed to be weakly spilling breaking waves which transform to a non-breaking wave regime after about 4-5 breaking waves. Given that the spilling breaking waves are identified before reflections have an influence on the wave breaking, the observed waves are classified as spilling breaking waves. In the numerical results, no change in the wave breaking regime is seen, with spilling wave breaking calculated for the entire duration of the simulation. In the case of waves in $d = 0.58$ m, the criteria by Yao et al. (2013) predict spilling breaking waves, whereas plunging breaking waves are observed in the experiments and the numerical results.

Table 2: Wave breaker classification for cases A1-A6 with $d = 0.52$ m

Case	A1	A2	A3	A4	A5	A6
T_0 (s)	3.933	3.294	1.985	2.206	1.356	1.439
H_0 (m)	0.015	0.024	0.040	0.032	0.064	0.060
H_I (m)	0.019	0.028	0.042	0.034	0.079	0.071
Galvin (1969)	N/A	N/A	plunging	plunging	plunging	plunging
Smith and Kraus (1990)	N/A	N/A	surging	surging	plunging	plunging
Yao et al. (2013)	non-breaking	non-breaking	spilling	spilling	plunging	plunging
Current experiments	non-breaking	non-breaking	spilling	spilling	plunging	plunging
Current simulations (wide domain)	non-breaking	non-breaking	spilling	spilling	plunging	plunging

Table 3: Wave breaker classification for cases B1-B6 with $d = 0.55$ m

Case	B1	B2	B3	B4	B5	B6
T_0 (s)	3.206	2.854	1.820	1.989	1.282	1.351
H_0 (m)	0.021	0.025	0.048	0.040	0.070	0.064
H_I (m)	0.024	0.028	0.051	0.042	0.094	0.081
Galvin (1969)	N/A	N/A	plunging	plunging	plunging	plunging
Smith and Kraus (1990)	N/A	N/A	surging	surging	plunging	plunging
Yao et al. (2013)	non-breaking	non-breaking	spilling	non-breaking	plunging	plunging
Current experiments	non-breaking	non-breaking	spilling	spilling	plunging	plunging
Current simulations (wide domain)	non-breaking	non-breaking	spilling	spilling	plunging	plunging

Table 4: Wave breaker classification for cases C1-C6 with $d = 0.58$ m

Case	C1	C2	C3	C4	C5	C6
T_0(s)	2.869	2.488	1.673	1.817	1.213	1.282
H_I (m)	0.028	0.031	0.055	0.048	0.064	0.067
H_0 (m)	0.031	0.033	0.062	0.052	0.100	0.095
Galvin (1969)	N/A	N/A	plunging	plunging	plunging	spilling
Smith and Kraus (1990)	N/A	N/A	surging	surging	plunging	spilling
Yao et al. (2013)	non-breaking	spilling	spilling	non-breaking	spilling	spilling
Current experiments	non-breaking	non-breaking	spilling	spilling	plunging	plunging
Current simulations (wide domain)	non-breaking	non-breaking	spilling	spilling	plunging	plunging

4.2 Grid convergence study and validation of the numerical model

A grid convergence study is carried out to determine the optimal grid size distribution using the non-uniform grid approach using the wider numerical domain with $y_{max} = 2.0$ m. Three simulations are carried out for the spilling breaking waves C3 with $725 \times 110 \times 55$, $1450 \times 220 \times 110$ and $1595 \times 242 \times 110$ cells, resulting in 4.4, 35.1 and 42.5 million cells respectively. The free surface elevations calculated at selected wave gauges for simulation C3 are presented in Fig.(3). The incident waves just over the toe of the seaward slope at P8, transformation of the waveform on the flat bed after shoaling on the seaward slope at P13 and P18 and the broken waves at P25 are seen in Figs.(3a), (3b), (3c) and (3d) respectively. The free surface elevations calculated with 35.1 million cells is seen to be similar to those calculated with 42.5 million cells, including in the case of the broken waves at P25. Therefore the grid resolution of $1450 \times 220 \times 110$ with 35.1 million cells is considered for the rest of the simulations in the study. A part of the domain with the stretched grid used in the study is shown in Fig.(4).

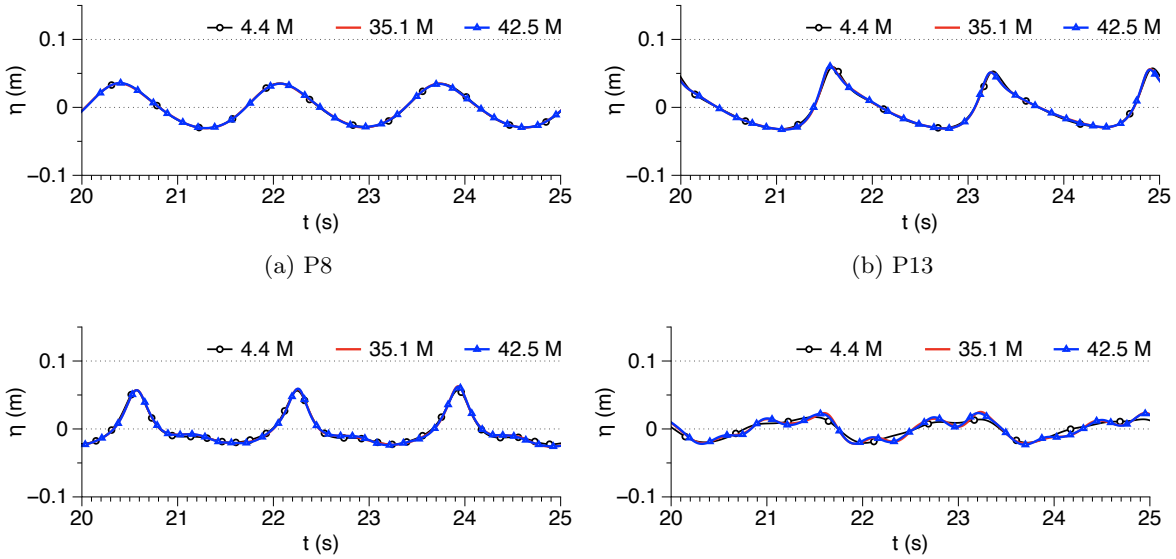

(a) P8 (b) P13

(c) P18 (d) P25

Figure 3: Grid convergence study for spilling breaking waves in simulation C3 with $T = 1.67$ s, $H = 0.062$ m, $d = 0.58$ m

Results for a non-breaking wave (C1) with $H = 0.031$ m and period $T = 2.87$s in water depth $d = 0.58$ m are presented with comparison to experimental data for in Fig.(5). Figures (5a) shows the incident waves before the structure at P/WG5 at $x = 3.409$ m, $y = 0.267$ m. The calculated and measured waves on the flat bed of the structure at $x = 6.493$ m at P/WG13, P/WG14, P/WG15 for $y = 0.822$ m, $y = 0.552$ and $y = 0.267$ are presented in Figs.(5b), (5c) and (5d) respectively. The effect of shoaling is seen from the asymmetry along the vertical axis in all the three figures. It is also observed that the asymmetry is highest at P/WG13 in shallower water ($d = 0.147$ m) and reduces as one moves towards deeper water at P/WG15 ($d = 0.303$ m). Further, free surface elevations at two locations along $y = 1.096$ m, P/WG17 and P/WG22, at $x = 7.681$ m and 8.850 m are presented in Figs.(5e) and (5f)

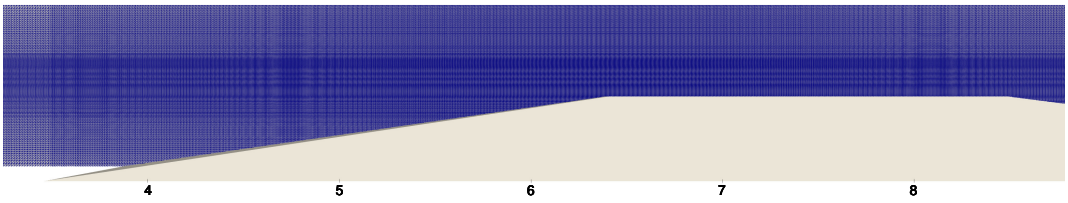

Figure 4: Part of the domain showing the stretched grid selected for the numerical simulations

respectively. Highly asymmetric waves are seen at these locations, but there is a lack of a steep wave crest and it clearly is a non-breaking wave, both in experiments and simulations. The agreement between the numerical and measured results is seen to be good. There are some differences that occur towards the end of the presented time series and are attributed to the reflection from the end of the flume in the experiments. The propagation of the waves in the numerical wave tank is presented in Fig.(6).

The results for the spilling breaking wave in case C3 with $H = 0.062$ m, $T = 1.67$ s in water depth $d = 0.58$ m are presented in Fig.(7). The same locations as for C1 are presented. Figure (7a) shows the waves approaching the structure at P/WG5. Three locations on the flat bed P/WG13, P/WG14 and P/WG15 are presented in Fig.(7b), (7c) and (7d) respectively. The vertical asymmetry of the free surface profile is the highest at P/WG13 in shallower water and the lowest at P/WG15 in deeper water. The free surface elevations at P/WG17 show a near vertical crest front profile indicating impending wave breaking. At P/WG22, the crest front steepness is reduced but the free surface profile indicates a steep non-breaking wave crest travelling post wave breaking. The numerical and measured results show good agreement, also around the region of wave breaking. The onset of a spilling breaking wave in the simulation at $x \approx 8.1$ m is presented in Fig.(8).

The results for a plunging breaking wave in case C5 with $H = 0.10$ m, $T = 1.21$ s in water depth $d = 0.58$ m are presented in Fig.(9). The wave incident on the structure calculated at P/WG5 is presented in Fig.(9a). The free surface elevations on the flat bed at P/WG13, 14 and 15 are presented in Fig.(9b), (9c) and (9d) respectively. Similar to C1 and C3 above, the vertical asymmetry is seen to reduce from P/WG13-P/WG15. A vertical crest front is seen in Fig.(9e) for P/WG17 indicating wave breaking. The agreement between the numerical and measured results is seen to be acceptable. Some differences are seen for P/WG13, 14 and 15, but the numerical results have a regular period and consistent amplitude. A Fourier analysis of the free surface elevations at the same locations as above is presented in Fig.(10). The wave energy is majorly concentrated in the fundamental frequency at P/WG5 as expected in Fig.(10a). The process of wave decomposition that leads to a reduction of the wave energy in the first harmonic and introduction of energy in the second and third harmonics is seen in Fig.(10b) and (10c) for P/WG13 and P/WG14 respectively. The effect of wave decomposition is lower at P/WG15 in deeper water over the side slope as seen in Fig.(10d). At the same time a reduction of the spectral amplitude is seen indicating a reduction in the energy reaching this location due to the interaction with the three-dimensional submerged bar. As a result of plunging wave breaking between P/WG13 and P/WG17, the spectral amplitudes are lower at P/WG17 and P/WG22 in Figs(10e) and (10f) respectively. The results show that the wave

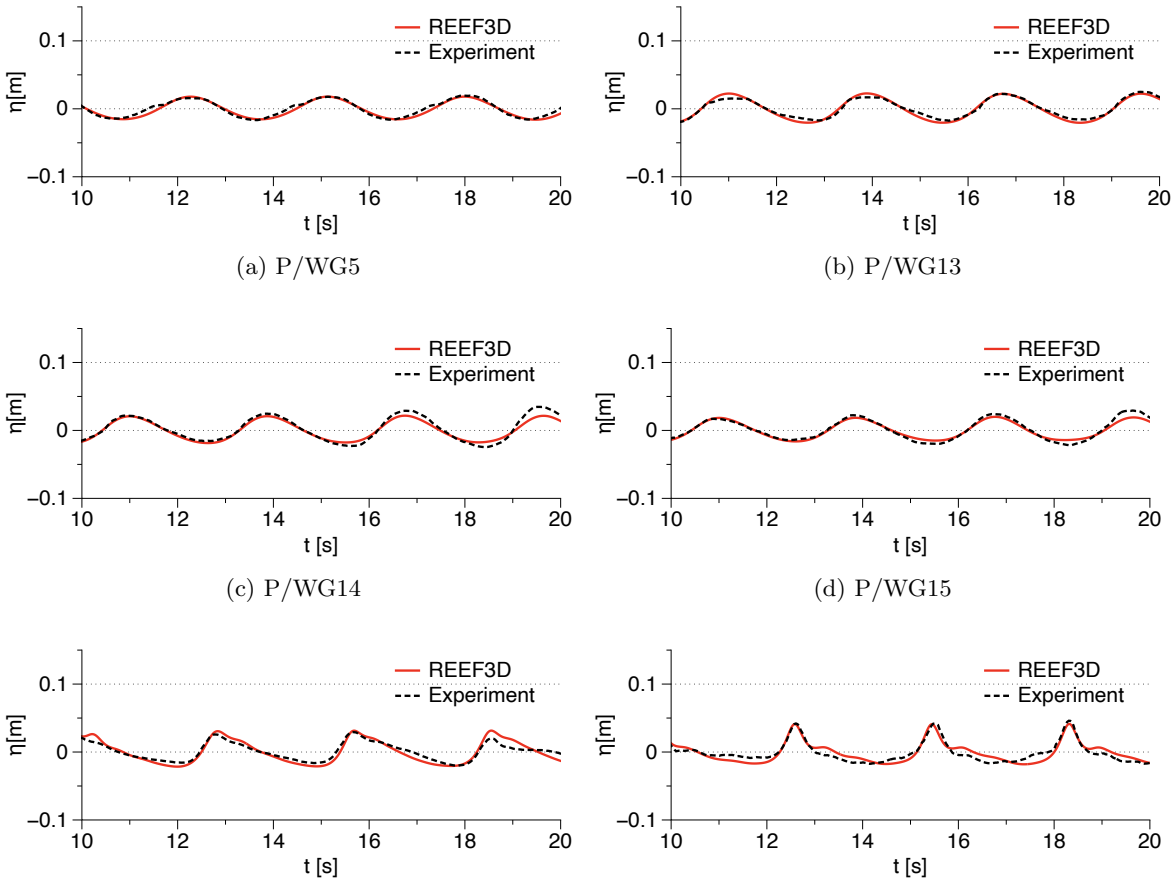

(a) P/WG5 (b) P/WG13

(c) P/WG14 (d) P/WG15

(e) P/WG17 (f) P/WG22

Figure 5: Comparison of numerical and experimental data for the free surface elevation at various locations for the non-breaking wave in simulation C1 with $T = 2.87$ s, $H = 0.031$ m, $d = 0.58$ m

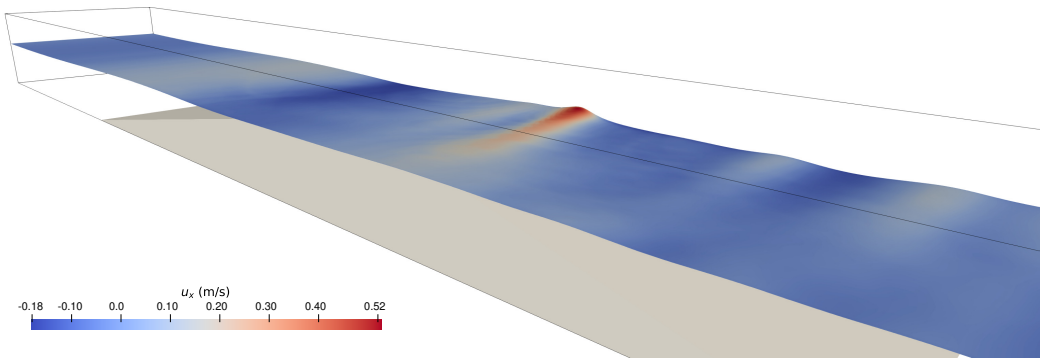

Figure 6: Part of the domain with the non-breaking wave in the numerical wave tank for simulation C1 with $T = 2.87$ s, $H = 0.0312$ m, $d = 0.58$ m

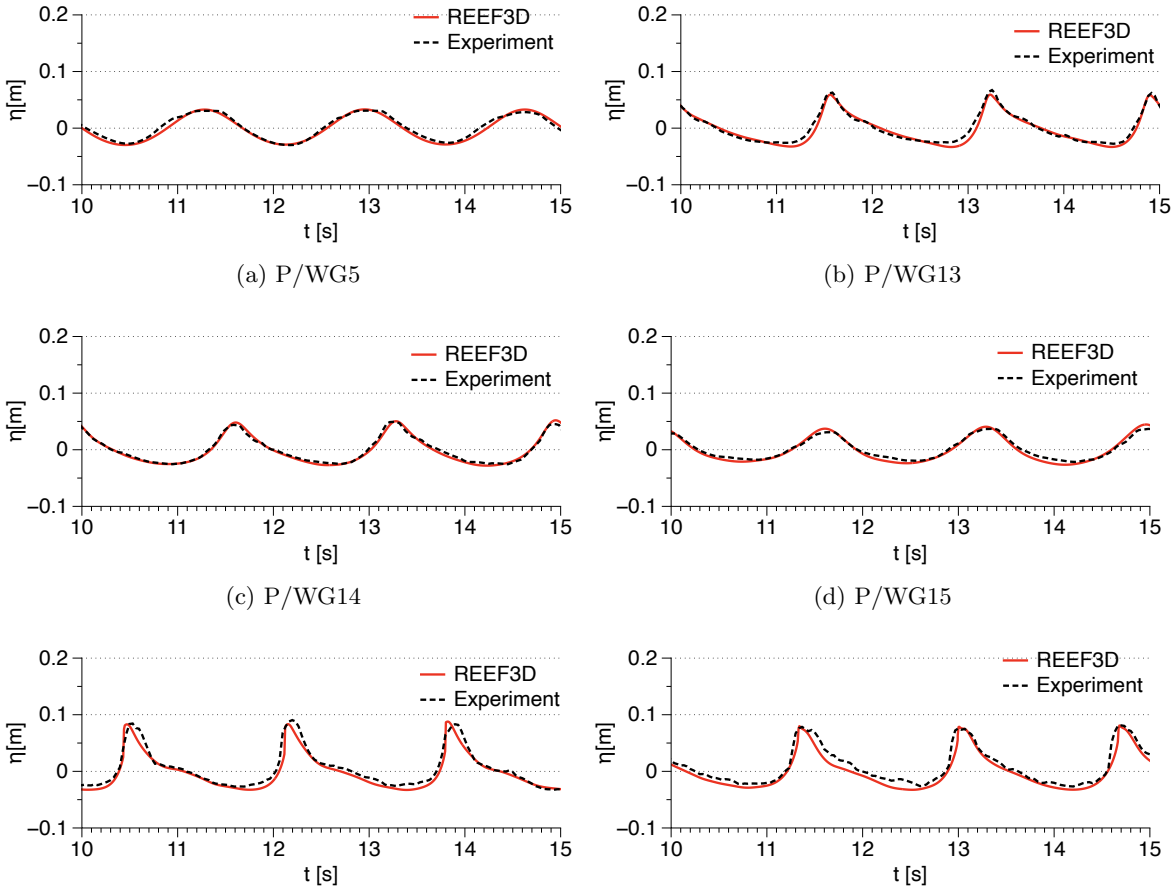

(a) P/WG5 (b) P/WG13

(c) P/WG14 (d) P/WG15

(e) P/WG17 (f) P/WG22

Figure 7: Comparison of numerical and experimental data for the free surface elevation at various locations for spilling breaking waves in simulation C3 with $T = 1.67$ s, $H = 0.062$ m, $d = 0.58$ m

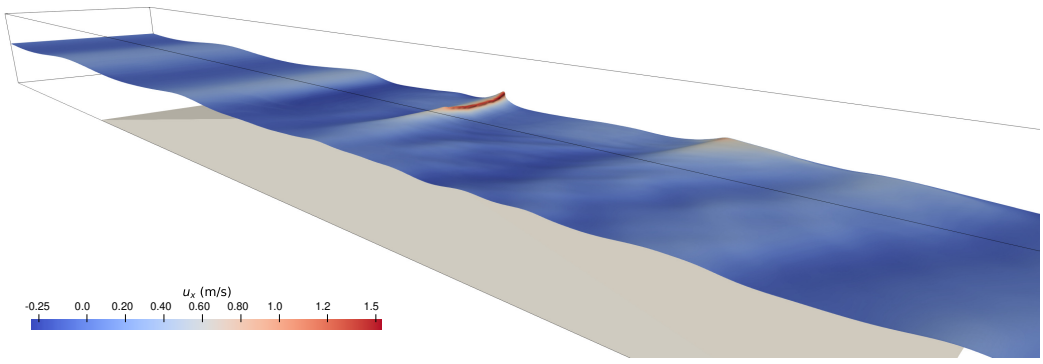

Figure 8: Part of the domain with the overturning wave crest for a spilling breaking wave in the numerical wave tank for simulation C3 with T=1.67 s, H=0.062 m, d=0.58 m

energy in the higher harmonics is well represented in the numerical model. The onset of a plunging breaking wave in the simulation at $x \approx 7.0$ m is presented in Fig.(11).

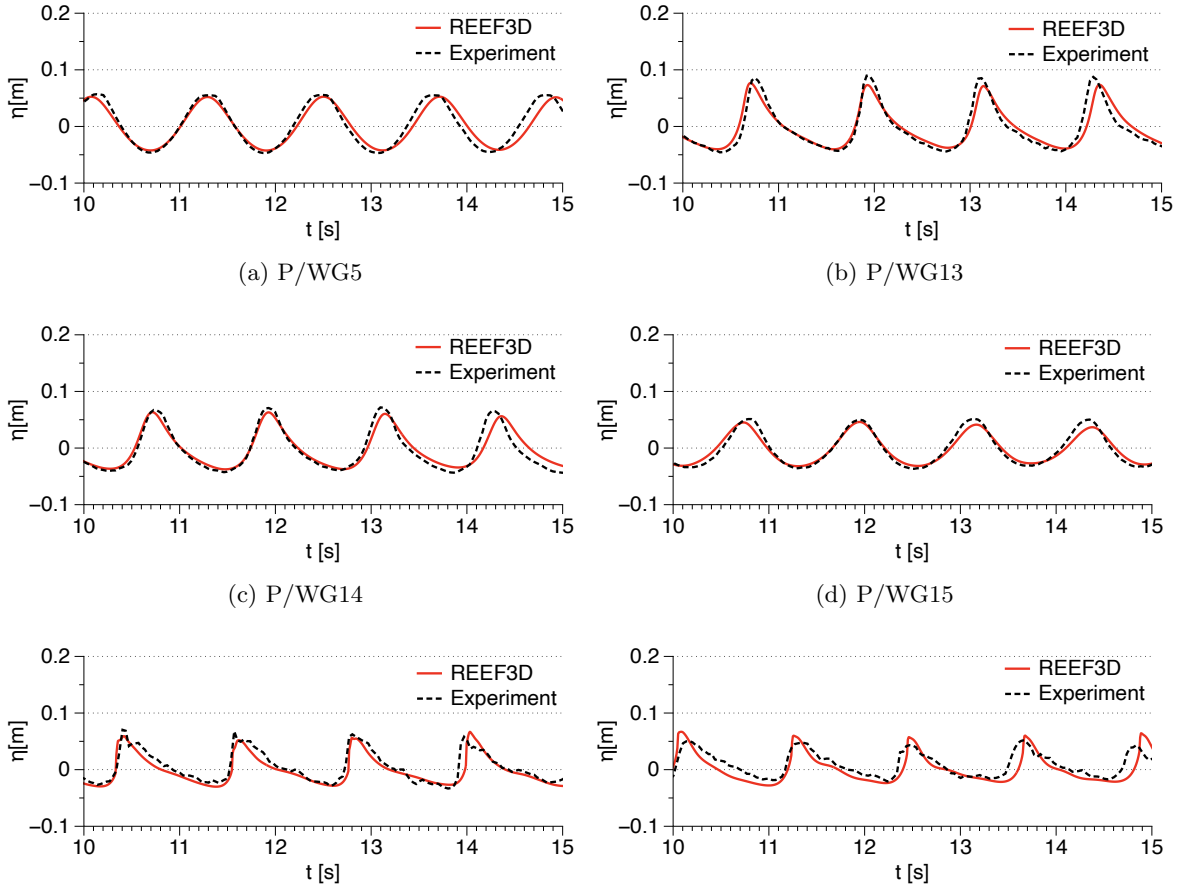

(a) P/WG5

(b) P/WG13

(c) P/WG14

(d) P/WG15

(e) P/WG17

(f) P/WG22

Figure 9: Comparison of numerical and experimental data for the free surface elevation at various locations for plunging breaking waves in simulation C5 with $T = 1.21$ s, $H = 0.10$ m, $d = 0.58$ m

While preliminary simulations were carried out using the numerical model to determine the wave characteristics and the dimensions of the submerged structure required to generate different breaking waves, the width of the tank was restricted due by the available physical facility. Due to the restricted width of the domain, there is a possibility of wall effects affecting the results. In order to reduce the possibility of such an outcome, the width of the numerical wave tank is increased to $y_{max} = 2.0$ m and 2.30 m to confirm a sufficient tank width to avoid the influence of the side wall. It is noticed that the difference between the results for free surface elevation in the narrow domain with y_{max}= 1.237 m and the wider domains with $y_{max} = 2.0$ m and 2.30 m is not very large in Fig.(12a). However, the wave crest front is steeper and due to the focus on the refraction effects in this study, a wider domain is considered. The calculated free surface elevations at P17 are identical for y_{max}= 2.0 m and 2.3 m in Fig.(12a). In addition, in the wider domains, the calculated free surface at P16 ($y = 1.80$ m) are quite

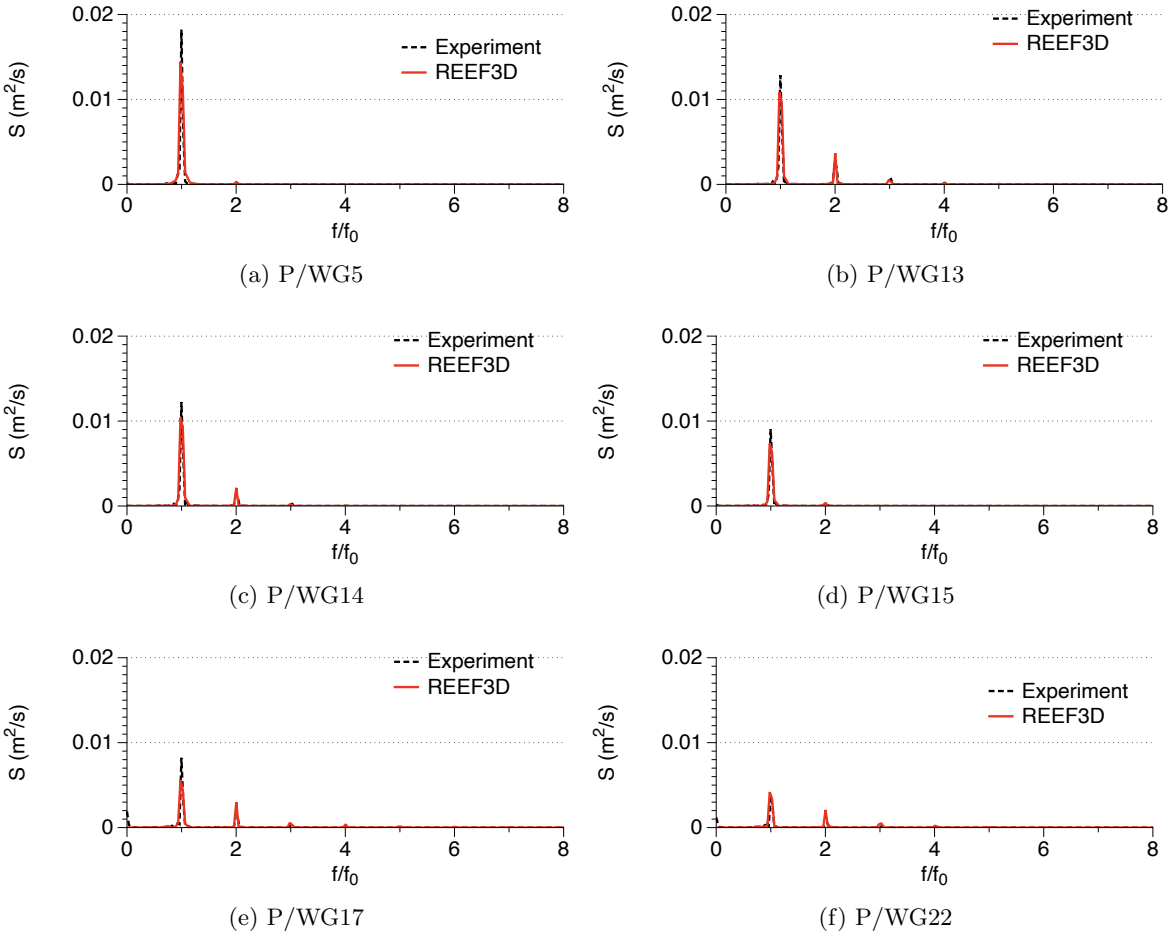

(a) P/WG5 (b) P/WG13

(c) P/WG14 (d) P/WG15

(e) P/WG17 (f) P/WG22

Figure 10: Comparison of the Fourier analysis of the free surface elevation at various locations for plunging breaking waves in simulation C5 with $T = 1.21$ s, $H = 0.10$ m, $d = 0.58$ m

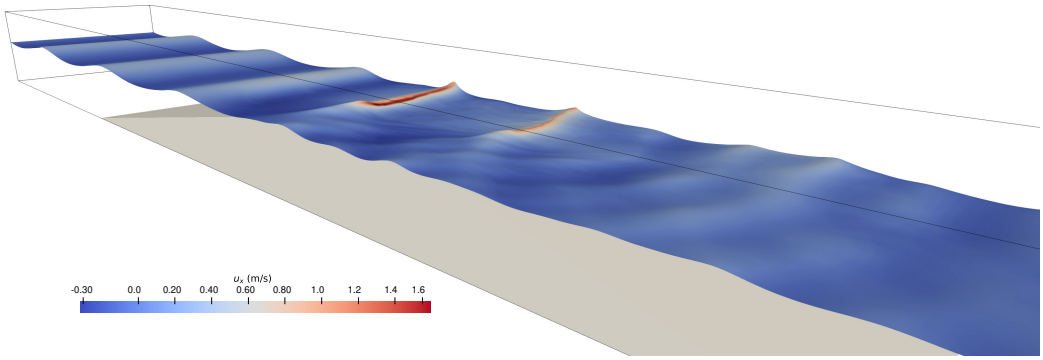

Figure 11: Overturning wave crest for a plunging breaking wave in the numerical wave tank for simulation C5 with $T = 1.21$ s, $H = 0.10$ m, $d = 0.58$ m

similar for y_{max}= 2.0 m and 2.3 m and also slighly lower than the free surface elevation at P17. Therefore, further analysis is carried out using numerical results from a y_{max}= 2.0 m wide domain.

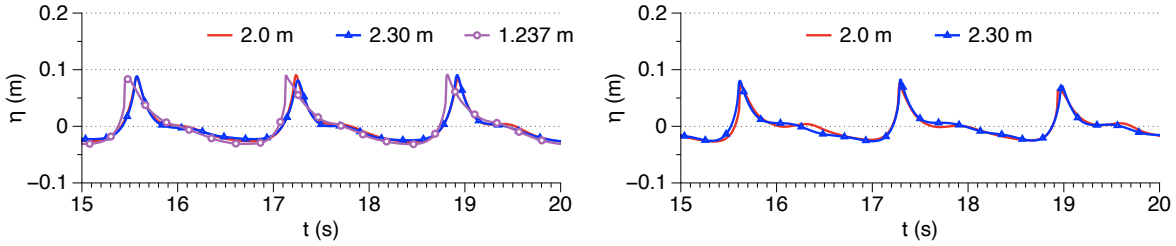

(a) P17 (b) P16

Figure 12: Effect on the width of the numerical wave tank on the free surface calculated at P17 and P16 for simulation C3

4.3 Wave decomposition and energy distribution

Non-breaking waves The decomposition of the waves into higher harmonics and the distribution of the wave energy over the numerical wave tank are further analysed using the Fourier transform of the calculated free surface elevations. In this section, the results for the Fourier analysis for selected locations: P12, P17, P20, P22 and P25, along with the zeroth spectral moment m_0 are presented and discussed. A time series of consisting of wave signals of about 40 s is used for this analysis. Location P12 is located in array #3, closer to the side wall and represents the state just before wave breaking. P17 and P20 are in array #4 and in the region of wave breaking. Furthermore, P17 is closer to the sidewall in shallower water, whereas P20 is above the side slope in deeper water. These provide an indication of the changes in the wave energy along the array. P22 and P25 from array #5 are chosen to represent the post-breaking scenario in shallower and deeper water respectively.

The results of the spectral analysis for cases A1, B1 and C1 are presented in Fig.(13). For all the locations in arrays #1 and #2 which are not presented here, all the wave energy is concentrated at the first harmonic. At P12 in array #3 shown in Fig.(13a), the wave energy is still mostly concentrated in the first harmonic $f/f_0 = 1$ in all three cases, with some energy appearing the second harmonic due to shoaling. On propagation to P17 in array #4, a slight reduction in the spectral amplitudes at the first harmonic and a corresponding increase in the second and the third harmonics is seen due to wave decomposition on the flat bed in Fig.(13b). In the same array, in deeper water at P20, a significant increase in the spectral amplitudes at the first harmonic is seen for B1 and C1 in Fig.(13c). The spectral amplitudes in shallower water at P22 in array #5 (Fig.(13d)) are similar to that for its collinear location in array #4, P17. In Fig.(13e) for P25, highly reduced spectral amplitudes in the first and second harmonics are seen for all the cases. In these cases, the spectral amplitudes are insignificant after the fourth harmonic for all cases at all locations and only P17 and P22 have noticeable values for the third and fourth harmonics. The wave energy is seen to mostly manifest in the first and second harmonics at all the locations in all the cases.

The zeroth spectral moment m_0 for the three cases is presented in Fig.(13f) as representation of the mean wave energy. The vertical dashed lines provide a visual guide to the different arrays in the domain. In array #1 (P1-P5), there is no significant change in the wave energy across the array as these are incident waves yet to interact with the structure. In array #2 (P6-P10), no major change is seen for A1, whereas a slight increase of energy along the array while moving towards shallow water is seen. In array #3 (P11-P15), a major change along the array is seen for C1 with a large increase in the wave energy at P11, close to the wall. This indicates a strong effect of combined shoaling and refraction over the structure resulting in increased free surface elevations in shallow water over the flat bed. For A1 and B1, no such dramatic increase is seen at this array. The major reason for the pattern seen for C1 stems from the fact that it is the steepest of the three waves and undergoes stronger shoaling over the seaward slope at this array. Using the time series of the free surface elevation at P11, the local wave steepness is approximated to be 0.009, 0.007 and 0.019 for A1, B1 and C1 respectively. A1 and B1 have similar wave steepness and show similar shoaling behaviour, weaker than that seen for C1 at this array. In the case of A1, the maximum m_0 is seen at P14 close to the upper edges of the seaward and side slopes due to the combined effect of shoaling and refraction. In the case of B1, the maximum value of m_0 is seen at P15 for this array due to a reflected wave travelling towards P20. In array #4 (P16-P20), A1 shows a similar behaviour as C1 in the previous array demonstrating the effect of combined shoaling and refraction. B1 follows a similar trend, but is influenced by some reflection, resulting in a higher value of m_0 at P20. The reflections in the flume are calculated to be strong in the case of C1 and to a lesser extent in the case of B1. This is due to the lack of wave energy dissipation in these non-breaking waves. This pattern is not calculated for the breaking waves presented in further sections. In array #5 (P21-P25), it is seen that the wave energy has a clear gradient along the array with the maximum in shallower water over the flat bed and minimum over deeper water over the side slope. In the simulations, it is seen that a the increased elevation seen at P11 for C1 and P12 for A1 and B1 continue to gradually gain in height during propagation towards P21. While P25 has no significant energy due to the process of reflection and refraction directing the waves towards P21.

Spilling breaking waves The results of the spectral analysis for cases A3, B3 and C3 are presented in Fig.(14). The spectral amplitudes for locations in array #1, not presented here, indicate slightly nonlinear incident waves with nonzero values for the second harmonic. The process of shoaling over the seaward slope results in an increase in the spectral amplitudes at the first and second harmonics for all cases. At P12 in array #3, some amount of wave decomposition is already seen with nonzero values up to the fifth harmonic for all the cases in Fig.(14a). In shallower water along array #4 at P17, significant values for the spectral amplitudes are seen up to the third harmonic in Fig.(14b) and nonzero values exist up to the eighth harmonic due to wave decomposition on the flat bed. In the case of C3, the spectral amplitudes at the second and the third harmonic are almost equal. The highly deformed free surface profile is seen in Fig.(7e). The process of refraction due to the side slope results in reduced spectral amplitudes at locations in deeper water such as P20 and P25 seen in Fig.(14c) and (14e). At P22 in shallower water over the flat bed, wave breaking results in reduced spectral amplitudes at all the frequencies and some energy is seen for the first two harmonics.

A study of the zeroth spectral moment m_0 in Fig.(14f) shows no major changes are seen

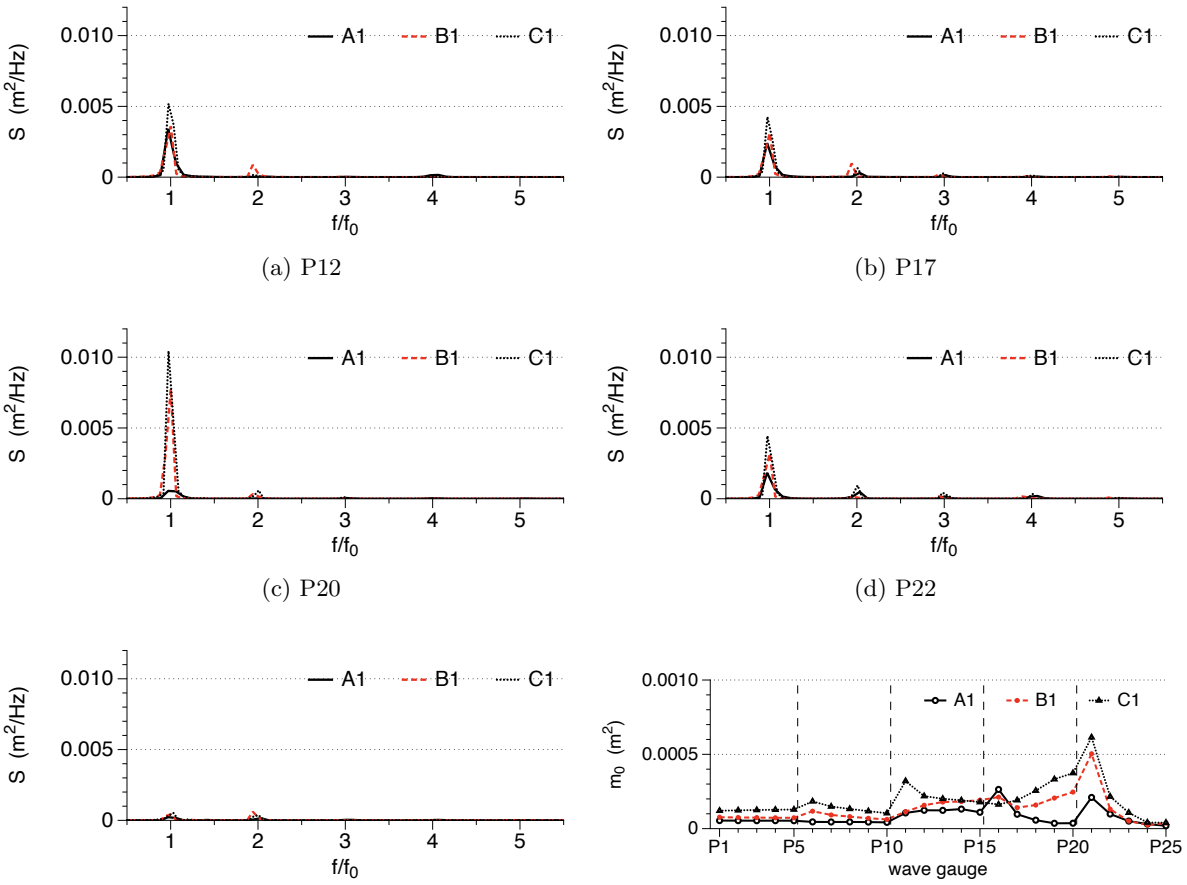

Figure 13: Spectral analysis of the free surface elevations at different locations in the numerical wave tank for non-breaking waves in A1, B1 and C1

along array #1 in any of the cases. A small gradient in the wave energy appears along array #2 for B3 and C3 with higher energies in shallower water than in deeper water due to shoaling over the seaward slope. For A3, this gradient between P6-P10 is quite pronounced and is soon followed by onset of spilling wave breaking in A3 around $x \approx 6.5$ m in shallow water over the flat bed. There is a large gradient in the energies for all the cases along array #3. For A3, P11 is situated at the onset of spilling wave breaking. For B3 and C3, the onset of spilling wave breaking is seen at $x \approx 6.7$ m and 7.3 m respectively. The formation of the steep wave crest front before breaking in these regions explains the increase in energy calculated at locations on the flat bed in array #3. The lower energy calculated at locations in deeper water in array #3 is due to the fact that there is no increase in the free surface elevations at locations with deeper water. In array #4, a peak in the wave energy is seen for all three cases in the region of P17. This is due the formation of a steep wave crest on the flat bed closer to the side slope, while steep non-breaking wave crests are seen in shallow water towards P16 and there is no significant increase in deeper water moving towards P20. In array #5, a peak emerges at P21 in shallow water again for all three cases. The steep non-breaking wave crest formed post-breaking that travels along the wall is seen to be the cause, which in the case of B3 and C3 dissipates at around $x \approx 8.8$ m and 9.6 m respectively. The broken wave is highly damped for A3 and also reflected in the low energies calculated for array #5. The process of shoaling and refraction over the side slope reduced the wave energy in the deeper water and close of zero energy is calculated at P25.

The results of the spectral analysis for cases A4, B4 and C4 are presented in Fig.(15). These cases are also identified as spilling breaking waves in the simulations. Similar to the group 3 spilling breaking waves presented previously, noticeable spectral amplitudes are seen up to the third harmonic at P12 in Fig.(15a). Since the waves in this group are slightly lower and longer than the previous group, the absolute values of the spectral amplitudes are slightly lower in the first harmonic. These longer waves seem to be more influenced by wave decomposition on the flat bed with more significant spectral amplitudes up to the fifth harmonic at P17 in Fig.(15b) compared to the waves in group 3. The spectral amplitudes at P20 and P25 in deeper water over the side slope have significant energy at the first harmonic and some nonzero, insignificant values for the second and third harmonics. At P22 in Fig.(15d), the first two harmonics have a similar spectral amplitude indicating strongly decomposed waves. The large reduction in the amplitudes compared to P17 indicates wave breaking in the region in between.

The trend in the calculated zeroth spectral moment m_0 in Fig.(15f) shares several similarities to that seen for group 3 above. The trend in the calculated values for arrays #1 and #2 are similar to that seen for group 3 above and for similar reasons. The distribution of the wave energy over arrays #3, #4 and #5 shows a similar pattern as well, with increase in energy away from the deeper water over the side slope. The onset of primary wave breaking for A4, B4 and C4 are identified to be at $x \approx 6.6$ m, 7.2 m, and 8.1 m respectively. A steep non-breaking wave crest propagates over the flat crest, which dissipates around $x \approx 9.4$ m, 9.5 m and 9.9 m for A4, B4 and C4 respectively.

Plunging breaking waves The results of the spectral analysis for the plunging breaking waves A5, B5 and C5 are presented in Fig.(16). The spectral amplitudes at arrays #1 and #2, not presented here, have nonzero values in the second harmonic signifying higher order incident waves. At P12 in array #3 presented in Fig16a, significant values for up to the third

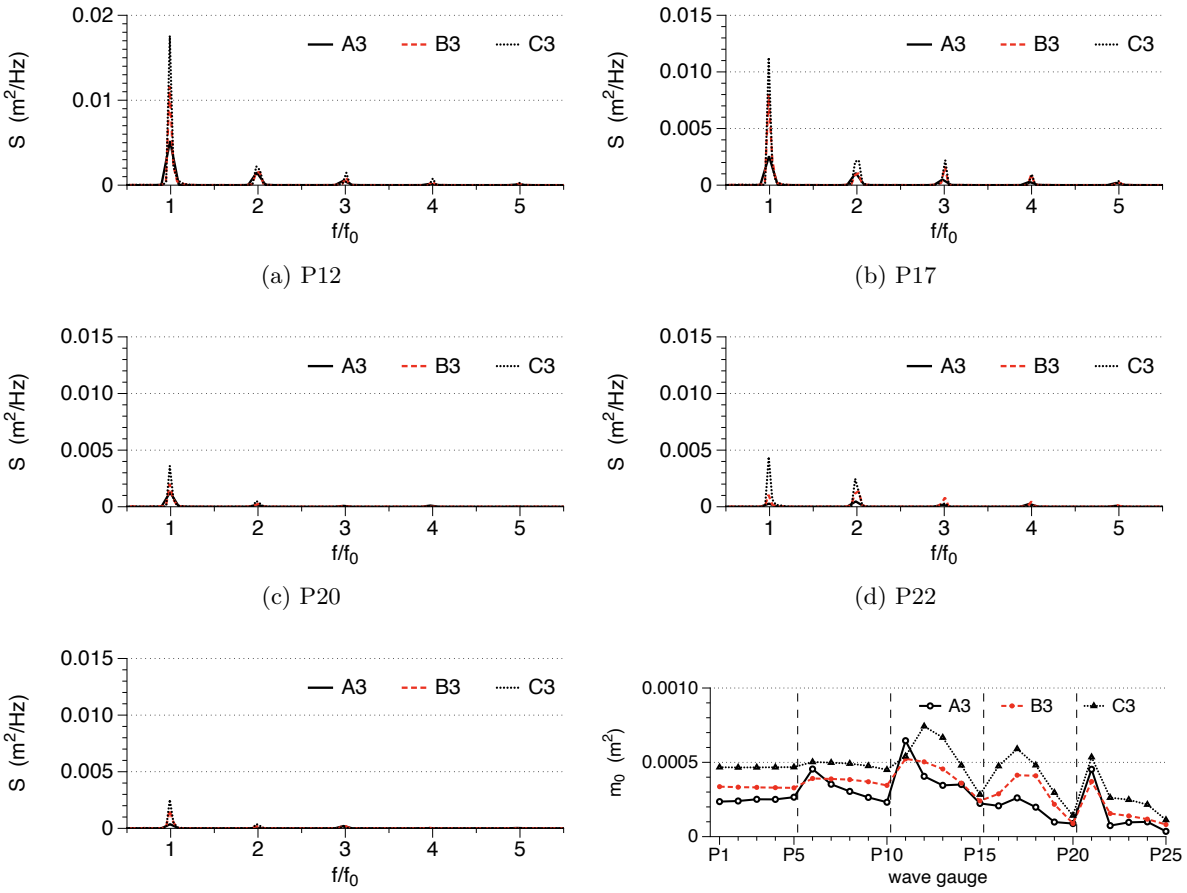

(a) P12 (b) P17

(c) P20 (d) P22

(e) P25 (f) m_0

Figure 14: Spectral analysis of the free surface elevations at different locations in the numerical wave tank for spilling breaking waves in A3, B3 and C3

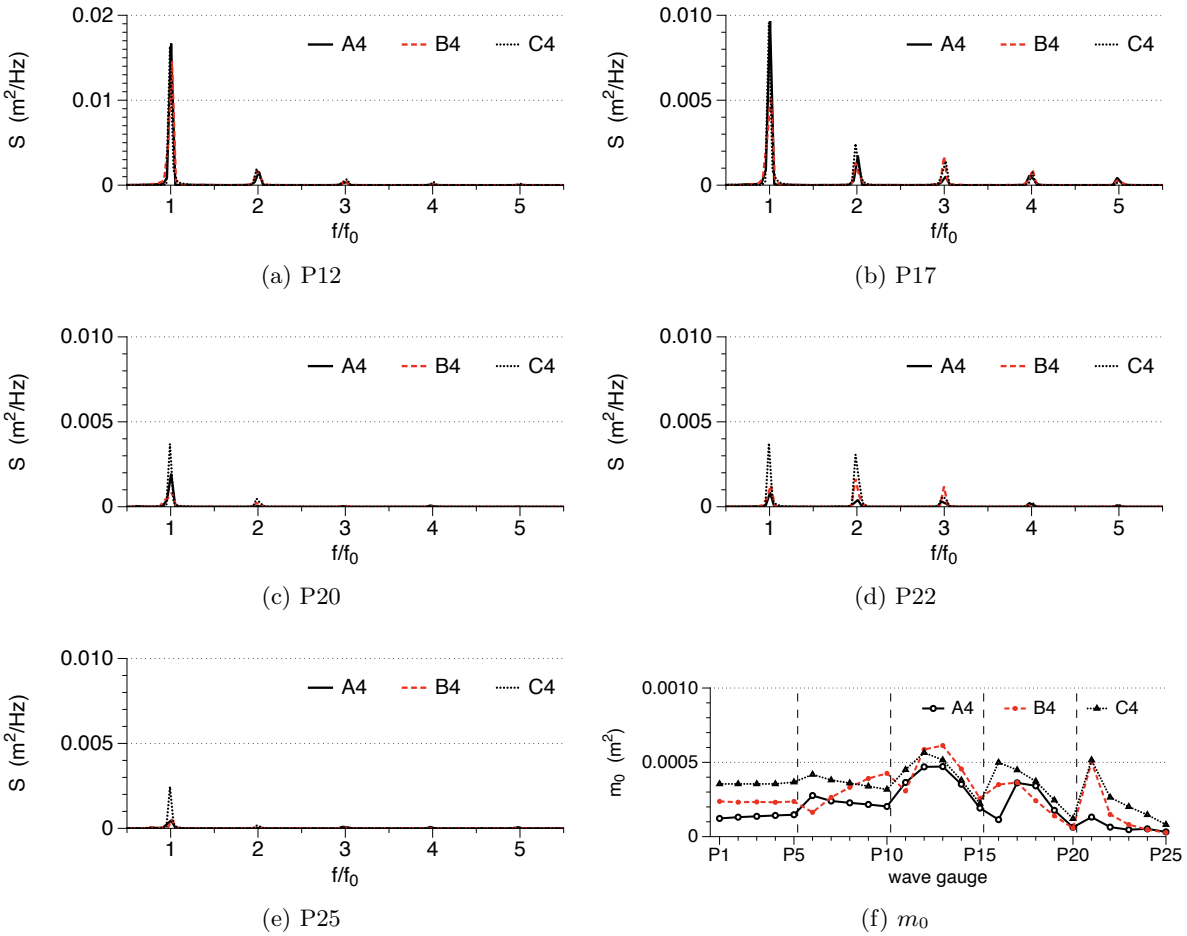

(a) P12 (b) P17

(c) P20 (d) P22

(e) P25 (f) m_0

Figure 15: Spectral analysis of the free surface elevations at different locations in the numerical wave tank for spilling breaking waves in A4, B4 and C4

harmonic are seen after the shoaling on the seaward slope. The waves in this group are the highest waves simulated in this study for the respective water depths. The waves show strong influence of shoaling and furthermore significant decomposition on the flat bed at P17 in array #4 as seen in Fig.(16b). The free surface elevation calculated in deeper water in array #4 at P20 shows a large reduction in the spectral amplitudes and presents some energy in the first two harmonics. In shallow water over the flat bed in array #5 at P22, the spectral amplitudes are largely reduced primarily in the first harmonic indicating wave breaking and have nonzero values up to the fifth harmonic. In deeper water over the side slope at P25 a small spectral amplitudes are seen for the first two harmonics.

The zeroth spectral moment m_0 calculated for these cases is presented in Fig.(16f). The variation of the wave energy for all the three waves for all the five arrays is seen to be quite similar in this case. No significant change is seen along array #1 and some increase in wave energy moving away from the side slope in array #2. The highest wave energy in array #3 is seen at P13 on the flat bed. Onset of plunging wave breaking occurs for A5, B5 and C5 at $x \approx 6.5$ m, 6.6 m and 6.9 m respectively, in the region $y = 0.6 - 1.0$ m justifying the maximum values of m_0 are seen at P13, while lower values are calculated for probes towards either wall. The plunging wave breaking results in a large amount of energy dissipation. Therefore, the post-breaking wave crests for these waves are smaller in height compared to the those seen for the spilling breaking waves above. The steep crest propagates along the centre of the flat bed resulting in the higher energies calculated for P17 and P18 in array #4 and P23 in array #5.

The results of the spectral analysis for cases A6, B6 and C6 are presented in Fig.(17). The incident wave heights for this group of plunging breaking waves are slightly lower and periods slightly longer than that for group 5 above. The distribution of the wave energies along the different arrays is seen to be similar to that of group 5. A noticeable difference is that more energy is preserved in the first harmonic in these cases compared to that seen for group 5 above. This can be attributed to slightly less dissipation of energy by plunging wave breaking of these slightly lower waves. Plunging wave breaking is seen at $x \approx 6.5$ m, 6.6 m and 6.8 m for A6, B6 and C6 respectively. This explains the peak in the wave energy seen at P12 and P13 in array #3 in Fig.(17f). A steep non-breaking wave crest is seen propagating in the region between wave breaking and array #4, which is highly dissipated by the time it reaches array #5.

4.4 Propagating wave front and direction

The three-dimensional submerged structure with slopes on both the stream wise and transverse directions results in a complex process of concurrent wave shoaling, refraction and breaking. The free surface contours in the different simulations are analysed to determine the change in the direction of the wavefront due to refraction. The extent of the overturning wave crest in each case is also investigated. The angle of propagation over the seaward slope α and the width of the overturning wave crest y' are defined in Fig.(18). Figure (18a) illustrates the propagation of the wave over the seaward slope and the refraction due to the side slope resulting in the rotation of the wavefront around $x = 6.0$ m. The angle of rotation α is determined from the tangent to the contour in this region. The extent of the steep non-breaking crest seen in A1 is measured as y'. Similarly, the rotation of the wavefront and the extent of the overturning wave crest in the case of spilling breaking waves in B3 and plunging

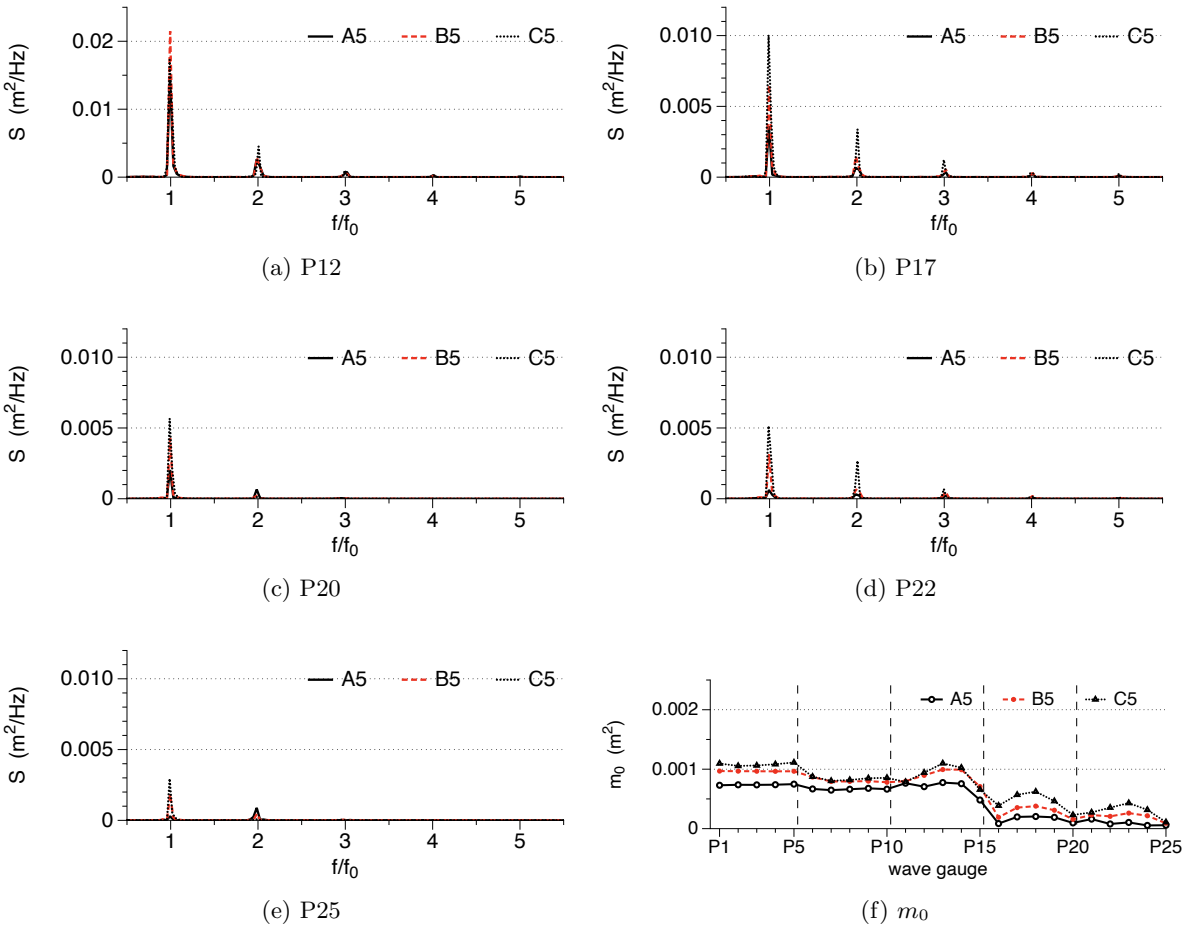

(a) P12 (b) P17

(c) P20 (d) P22

(e) P25 (f) m_0

Figure 16: Spectral analysis of the free surface elevations at different locations in the numerical wave tank for plunging breaking waves in A5, B5 and C5

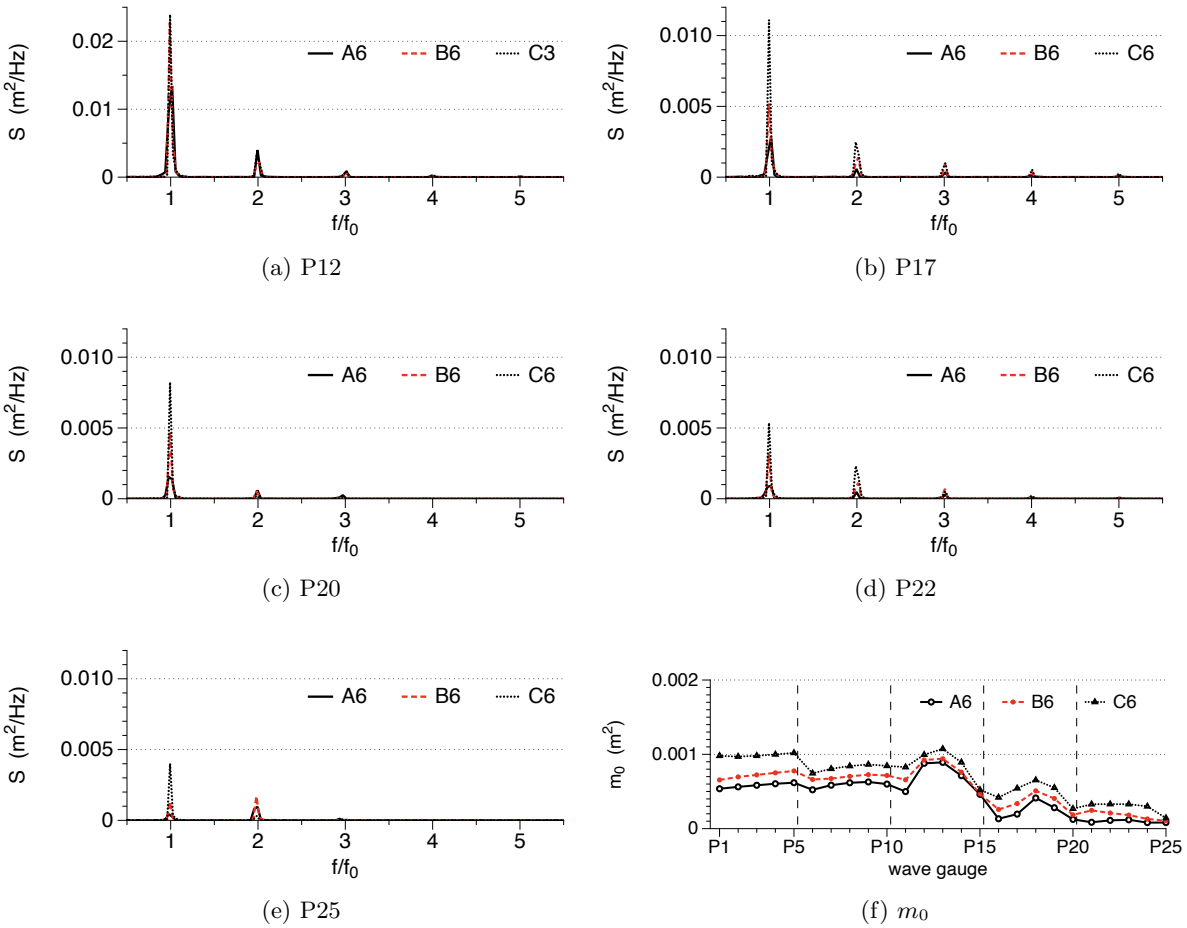

(a) P12 (b) P17

(c) P20 (d) P22

(e) P25 (f) m_0

Figure 17: Spectral analysis of the free surface elevations at different locations in the numerical wave tank for plunging breaking waves in A6, B6 and C6

breaking waves in C6 are demonstrated in Figs.(18b and 18c). The values of α and y' for all the simulations in study are listed in Table (5) along with the type of breaking observed and the breaking point. The breaking point is the position at which the wave crest front becomes vertical. In the case of non-breaking waves, the location of the steep non-breaking wave crest is provided.

The analysis indicates that the non-breaking waves in shallower water depths A1 and B1 are the waves refract the most, while the plunging breaking waves refract the least. Also, for the non-breaking and spilling breaking waves, the amount of refraction is inversely related to the water depth. Relating these observations to the wave characteristics, it can be concluded that longer waves in shallower water are refracted more. Despite the difference in the amount of refraction in each case, the calculated values of α lie within a narrow band of 5-13°.

The width of the steep non-breaking wave crest for A1, B1 and C1 are of the order 0.5 m and formed close to the wall at $y = 2.0$ m. In the case of A1, some amount of spilling breaking is identified by the authors in the last 0.1 m close to the wall but this is ignored purely as a wall effect. The effect of strong refraction and lack of wave breaking results in the wave energy moving towards the wall in these cases. Reflection towards deeper water for B1 and C1 is discussed in previous sections. In the case of breaking waves, it is seen that spilling breaking occurs over a shorter width of the domain compared to plunging breaking. The steep wave crest front resulting in spilling breaking waves are about 1-1.2 m wide, whereas for the plunging breaking waves they are about 1.3-1.5 m wide. The overturning wavefront is not normal to positive x-axis due to the preceding refraction as seen in Fig.(18) around $x \approx 7$ m. The onset of wave breaking is first seen with a steep overturning crest formed in the region $y = 0.6 - 1.2$ m. Post breaking, the steep non-breaking wave crests continue to propagate in a similar manner, justifying the energy distribution calculated for the different arrays in the previous section. Past the submerged structure, the highly dissipated wavefront moves in the direction towards the side slope as indicated by the lower elevations presented past $x = 9$ m in Fig.(18).

Table 5: Characteristics of the wavefront in the numerical wave tank

Case	breaking type	breaking point (m)	α (°)	y' (m)
A1	non-breaking	8.5	13	0.40
B1	non-breaking	8.6	11	0.43
C1	non-breaking	8.7	6	0.50
A3	spilling	6.5	14	1.23
B3	spilling	6.7	8	1.23
C3	spilling	7.3	7	1.05
A4	spilling	6.6	13	1.22
B4	spilling	7.2	7	1.12
C4	spilling	8.1	9	0.95
A5	plunging	6.5	6	1.53
B5	plunging	6.6	6	1.50
C5	plunging	6.9	8	1.46
A6	plunging	6.5	7	1.45
B6	plunging	6.6	7	1.56
C6	plunging	6.8	5	1.36

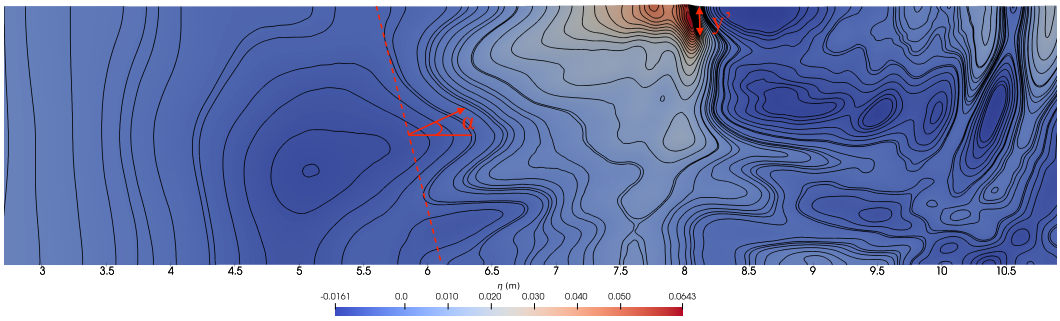

(a) A1, $H_I = 0.019$ m, $T = 3.933$ s

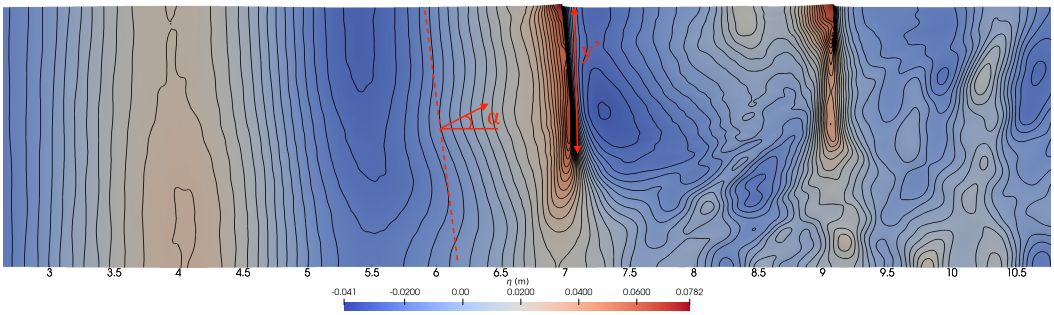

(b) B3, $H_I = 0.051$ m, $T = 1.820$ s

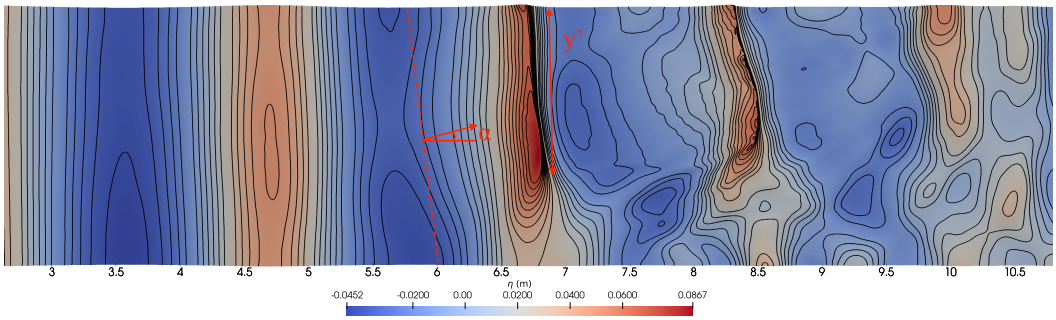

(c) C6, $H_I = 0.095$ m, $T = 1.282$ s

Figure 18: Free surface elevation contours in cases A1, B3 and C6 at onset of wave breaking illustrating the angle over the seaward slope α and the width of the overturning wave crest y'.

5 Conclusion

The propagation of waves over a three-dimensional obstacle in a wave flume is investigated both through experiments and numerical modelling. The breaking waves are classified based on criteria available in literature for wave breaking over two-dimensional structures. The measurements are used to validate the numerical wave tank in the open-source CFD model REEF3D and the investigation of the wave decomposition, energy distribution, wave direction and overturning crest formation is investigated numerically. The investigations show that a local water-depth dependent criterion to classify wave breaking is reasonably applicable to predict wave breaking over a three-dimensional structure. The study demonstrates the complex combined shoaling, refraction and breaking phenomena, and quantifies the wave decomposition over the flat bed and the energy transfer in the lateral direction due to a complex bottom. The following conclusions can be drawn from the analysis of the measured and calculated results presented above:

1. The classification based on Galvin (1969) and Smith and Kraus (1990) predict plunging and surging breaking waves respectively for spilling breaking waves that are observed in the experiments and the calculated numerically.

2. The classification based on Yao et al. (2013) mostly agree with the observed and calculated wave breaking. Exceptions are seen for the cases with deepest water depth in study where weak spilling breakers are classified as non-breaking and plunging breakers are classified as spilling.

3. Wave decomposition into higher harmonics is seen for all the cases over the flat bed. In deeper water along the same lateral direction, the wave energy is seen to be concentrated in the first two harmonics.

4. The variation of the wave energy along the lateral direction is seen to be similar for similar wave breaking types. It is also observed that the wave energy is majorly transferred away from the sides slope in all the cases.

5. The longer period non-breaking waves are seen to be the most effected by wave refraction and most of the wave energy is directed away from the side slope, leading to the formation of a steep non-breaking wave crest. The steep crest is formed close to the wall within 25% of the domain width and propagates along the wall before it is dissipated.

6. The spilling breaking waves form a steep crest over about 50% of the domain width before wave breaking. A steep non-breaking wave crest is formed post-breaking and propagates as such over the bar.

7. The plunging breaking waves form a steep crest over about 75% of the domain width before wave breaking. Most of the wave energy is lost in the breaking process and the free surface elevations following breaking are significantly reduced.

Further studies can shed more light on the relationship between the extent of the steep crest and the side slope, the extent of the side slope and the amount of refraction, and finally the effect of the three-dimensional geometry on the type of wave breaking.

Acknowledgements

The computations were performed on resources provided by UNINETT Sigma2 - the National Infrastructure for High Performance Computing and Data Storage in Norway under project no. NN2620K.

References

Aggarwal, A., Bihs, H., Myrhaug, D. and Alagan Chella, M. (2019*a*). Characteristics of breaking irregular wave forces on a monopile. *Applied Ocean Research*, **90**, 101846.

Aggarwal, A., Bihs, H., Shirinov, S. and Myrhaug, D. (2019*b*). Estimation of breaking wave properties and their interaction with a jacket structure. *Journal of Fluids and Structures*, **91**, 102722.

Alagan Chella, M., Bihs, H. and Myrhaug, D. (2019). Wave impact pressure and kinematics due to breaking wave impingement on a monopile. *Journal of Fluids and Structures*, **86**, 94–123.

Alagan Chella, M., Bihs, H., Myrhaug, D. and Muskulus, M. (2016). Hydrodynamic characteristics and geometric properties of plunging and spilling breakers over impermeable slopes. *Ocean Modelling, Virtual Special Issue: Ocean Surface Waves*, **103**, 53–72.

Battjes, J.A. (1974). Surf similarity. In: *Proc.,* 14*th International Conference on Coastal Engineering, Copenhagen, Denmark*, 466–480.

Beji, S. and Battjes, J.A. (1993). Experimental investigation of wave propagation over a bar. *Coastal Engineering*, **19**, 151–162.

Bihs, H., Kamath, A., Alagan Chella, M., Aggarwal, A. and Arntsen, Ø.A. (2016). A new level set numerical wave tank with improved density interpolation for complex wave hydrodynamics. *Computers & Fluids*, **140**, 191–208.

Blenkinsopp, C.E. and Chaplin, J.R. (2008). The effect of crest submergence on wave breaking over submerged slopes. *Coastal Engineering*, **55**, 967–974.

Engsig-Karup, A.P., Hesthaven, J.S., Bingham, H.B. and Warburton, T. (2008). Dg-fem solution for nonlinear wave-structure interaction using boussinesq-type equations. *Coastal Engineering*, **55**(3), 197–208.

Galvin, C.J. (1969). Breaker travel and choice of design wave height. *Journal of the Waterways and Harbors Division*, **95**(2), 175–200.

Grilli, S.T., Guyenne, P. and Dias, F. (2001). A fully non-linear model for three-dimensional overturning waves over an arbitrary bottom. *International Journal for Numerical Methods in Fluids*, **35**(7), 829–867.

Johnson, H.K. (2006). Wave modelling in the vicinity of submerged breakwaters. *Coastal engineering*, **53**(1), 39–48.

Kamath, A., Fleit, G. and Bihs, H. (2019). Investigation of free surface turbulence damping in rans simulations for complex free surface flows. *Water*, **11**(3), 456.

Kjeldsen, S. and Myrhaug, D. (1978). *Kinematics and dynamics of breaking waves*. River and Harbour Laboratory (NHL) — The Norwegian Institute of Technology.

Kouvaras, N. and Dhanak, M.R. (2018). Machine learning based prediction of wave breaking over a fringing reef. *Ocean Engineering*, **147**, 181–194.

Larsen, B.E., van der Zanden, J., Ruessink, G. and Fuhrman, D.R. (2020). Stabilized rans simulation of surf zone kinematics and boundary layer processes beneath large-scale plunging waves over a breaker bar. *Ocean Modelling*, **155**, 101705.

Liu, S., Ong, M.C., Obhrai, C., Gatin, I. and Vukčević, V. (2020). Influences of free surface jump conditions and different k- ω sst turbulence models on breaking wave modelling. *Ocean Engineering*, **217**, 107746.

Martins, K., Blenkinsopp, C., Deigaard, R. and Power, H.E. (2018). Energy dissipation in the inner surf zone: New insights from li dar-based roller geometry measurements. *Journal of Geophysical Research: Oceans*, **123**(5), 3386–3407.

Menter, F.R. (1992). Two-equation eddy-viscosity turbulence models for engineering applications. *The American Institute of Aeronautics and Astronautics Journal*, **32**, 1598–1605.

Miquel, A.M., Kamath, A., Alagan Chella, M., Archetti, R. and Bihs, H. (2018). Analysis of different methods for wave generation and absorption in a cfd-based numerical wave tank. *Journal of Marine Science and Engineering*, **6**(2), 73.

Naot, D. and Rodi, W. (1982). Calculation of secondary currents in channel flow. *Journal of the Hydraulic Division, ASCE*, **108**(8), 948–968.

Roy, T.L. (2018). *Experiments for Waves Breaking Over a Three-Dimensional Submerged Bar*. Master's thesis, Florida Atlantic University.

Smith, E.R. and Kraus, N.C. (1990). Laboratory study on macro-features of wave breaking over bars and artificial reefs. Technical Report CERC-TR-90-12, Coastal Engineering Research Center.

Stelling, G. and Zijlema, M. (2003). An accurate and effcient fnite-difference algorithm for non-hydrostatic free-surface fow with application to wave propagation. *International Journal for Numerical Methods in Fluids*, **43**, 1–23.

Sutherland, P. and Melville, W.K. (2015). Field measurements of surface and near-surface turbulence in the presence of breaking waves. *Journal of Physical Oceanography*, **45**(4), 943–965.

Ting, F.C.K. and Kirby, J.T. (1996). Dynamics of surf-zone turbulence in a spilling breaker. *Coastal Engineering*, **27**, 131–160.

Yao, Y., Huang, Z., Monismith, S.G. and Lo, E.Y. (2013). Characteristics of monochromatic waves breaking over fringing reefs. *Journal Coastal Research*, **29**(1), 94–104.